Assessment of Acid and Thermal Oxidation Treatments for Removing sp^2 bonded Carbon from the Surface of Boron Doped Diamond

Samuel J. Cobb,[a,d,e,+] Fraser H. J. Laidlaw,[b,d,+] Geoff West,[c] Georgia Wood,[a,d] Mark E. Newton,[b] Richard Beanland[b] and Julie V. Macpherson[a,*]

a) Department of Chemistry, University of Warwick, Coventry, CV4 7AL, UK

b) Department of Physics, University of Warwick, CV4 7AL, UK

c) Warwick Manufacturing Group, University of Warwick, CV4 7AL, UK

d) Diamond Science and Technology CDT, University of Warwick, CV4 7AL, UK

e) Current address Department of Chemistry, University of Cambridge, CB2 1EW

Abstract

The presence of sp^2 bonded carbon on a diamond or doped diamond surface, as a result of growth or processing, can affect material properties negatively, hence removal processes must be developed. Using boron doped diamond (BDD) we investigate the effectiveness of different removal methods via electrochemistry and transmission electron microscopy. We focus on two BDD surfaces, one processed by ns laser micromachining and the second which contains sp^2 bonded carbon as a result of chemical vapour deposition (CVD) growth. After micromachining a layer of ordered graphite sits on the BDD surface, topped by fissured amorphous carbon (total thickness ~ µm). Oxidative acid treatment at elevated temperature cannot remove all the sp^2 bonded carbon and much smaller clusters of perpendicularly-orientated graphite (10's nm), capped with a thinner layer of amorphous carbon – that we term "denatured graphite" – remain. In contrast, thermal oxidation in air at 600 °C is capable of all cluster removal, and can also be used to remove sp^2 bonded carbon from CVD-grown BDD. Such understanding is important to any application where sp^2 bonded carbon resulting from CVD growth or laser processing is detrimental for the intended application, e.g. in diamond quantum technology, photonics and electrochemistry.

Keywords:

Boron-doped Diamond (BDD), Electrochemistry, Laser Micromachining, Denatured Graphite, Oxidation, Transmission Electron Microscopy (TEM), Scanning Transmission Electron Microscopy (STEM), Electron Energy Loss Spectroscopy (EELS)

Introduction

Diamond for technological applications is traditionally grown using chemical vapour deposition (CVD) in both single crystal and polycrystalline form. The former on single crystal supports (homoepitaxy) and the latter on non-diamond (heteroepitaxy) substrates. Both can be grown in both thin and thick film format,[1,2] with the advantage thick films can be removed from the support and handled as freestanding material. The common conductive form of diamond, heavily boron doped diamond (BDD), is most often used for electrochemical applications.[3]

To fully realise the range of possible applications it is important the material can be processed into structures appropriate for the intended use. In this regard, techniques such as dry/wet etching[4] and nanosecond (ns)-laser micromachining are commonly employed.[5–8] The latter is extremely useful for cutting and structuring wafer scale diamond (and BDD) films into much smaller, useable geometries.[9–12] ns-laser micromachining does however, introduce non-diamond carbon into a laser cut diamond surface, [9,12–21], unlike dry/wet etching.[22] This is attributed to thermal damage by the laser beam, resulting in a solid to solid conversion of diamond to graphite.[23] Sublimation of the resulting graphite can also occur.[23] This process repeats, on the timescale of the ns-laser pulse.[24] Transmission electron microscopy (TEM) of the laser cut surface reveals a highly ordered graphitic carbon layer[9,15] sandwiched between bulk diamond at the bottom and amorphous carbon at the top[9,15,17]. More costly femtosecond (fs)-laser machining methods can decrease sp^2 bonded carbon production, due to diamond ablation occurring without preceding graphitization,[25–27] however, this is only true under low fluence conditions which can lead to slow material removal rates. Many fs studies in fact demonstrate the creation of sp^2 bonded carbon after ablation.[28–30] Interestingly, similar issues of sp^2 bonded carbon surface contamination also exist in the diamond nanoparticle (NP) field where the synthesis methods result in NPs covered in a layer of graphitic-like carbon.[31,32]

In certain cases, having sp^2 bonded carbon present at the surface of the diamond is advantageous. This has been shown particularly for BDD, with regard to specific electrochemical applications. sp^2 bonded carbon improves the electrocatalytic activity of a BDD electrode towards important reactions such as oxygen reduction[33] and advanced oxidation processes.[34] sp^2 bonded carbon also possesses a wider range of surface functional groups, compared to diamond, some of which, e.g. quinones, are electroactive and can be used for voltammetric pH sensing [13,35]. sp^2 bonded carbon can also be introduced during the

CVD growth process and is especially prevalent during thin film growth (e.g. nanocrystalline diamond) and/or at high boron doping levels.[36][37] It is, however, an uncontrolled process and the surface content / spatial location of the sp^2 bonded carbon is difficult to control. This contrasts with ns-laser micromachining where sp^2 bonded carbon structures can be written in the surface with a spatial resolution limited only by the laser optics, typically on the micron scale. For example, ns-laser techniques have been used to create arrays of micro-spots of sp^2 bonded carbon on a BDD electrode in order to increase the electrochemical sensitivity of the electrode towards pH,[13,35] dissolved oxygen[33] and hypochlorite[38]. sp^2 bonded carbon creation is also possible using ion implantation via the creation of defects in diamond, which when appropriately annealed, graphitise. In this way sp^2 bonded carbon microarray electrodes in diamond have been created for the detection of neurotransmitters.[39,40]

Nonetheless, for many applications of diamond (and BDD) removal of any processing-created or growth related forms of sp^2 bonded carbon at the surface of the material is important. In this paper we first examine the effectiveness of two different oxidative treatments at removing surface sp^2 bonded carbon created during the ns-laser micromachining process. We focus on high temperature (>200 ^{o}C) oxidation in sulfuric acid with added potassium nitrate, used as a common cleaning procedure for diamond/BDD[41] and high temperature (up to 600^{o}C) thermal oxidation in air. Both represent cheaper, more accessible alternatives, to employment of a hydrogen plasma system, which can be used for sp^2 bonded carbon removal.[42,43] We use cross-section high resolution TEM and Electron Energy Loss Spectroscopy (EELS) to investigate the interfacial structure of the material after both ns-laser machining (ablation), and the two different oxidative treatments. Raman microscopy is not surface sensitive enough for this study as it penetrates several microns into the material[44]. We focus on BDD as due to its conducting nature, the electrochemical signature of quinone groups associated with surface integrated sp^2 bonded carbon, [21] can also be used to provide information on the effectiveness of the different treatments. However, our conclusions can extend to laser-processed diamond materials in general for use in e.g. quantum technology and photonic applications. Finally, we investigate how well the methods assessed translate to sp^2 bonded surface carbon produced as a result of the CVD synthesis process.

Materials and methods

Materials

All solutions were prepared from Milli-Q water (Millipore Corp.), resistivity 18.2 MΩ cm at 25 °C. For ns-laser micromachining studies, electroanalysis grade BDD was used (grown using CVD by Element Six (E6) Ltd., Harwell, UK) which contains minimal sp^2 content, is freestanding (370 µm thick), mechanically polished to ~ nm growth face roughness and metallically doped, ca. 3×10^{20} boron atoms cm^{-3}.[45] For as-grown electrode studies, microcrystalline BDD, on a silicon substrate (Condias GMBH, Germany) was employed. Capacitance and solvent window measurements were performed in 0.1 M potassium nitrate (KNO_3, Fischer Scientific) solution. For electrochemical quinone surface coverage (Γ) measurements, the electrode was cycled in 0.1 M H_2SO_4 as described previously[21] to ensure a consistent oxygen surface termination. Γ was measured in a pH 2 (measured using a SevenEasy pH meter, Mettler Toledo) Carmody buffer, prepared using boric acid (99.97%, Sigma Aldrich), citric acid (≥99.5%, Sigma Aldrich) and tertiary sodium phosphate (≥95%, Sigma Aldrich).[46]

Electrode preparation

For all ns-laser micromachining studies, BDD plates were cut from the wafer and the growth face subjected to laser machining, in air, using a 355 nm Nd:YAG laser micromachiner (E-355-ATHI-O system, Oxford Lasers Ltd. UK) with a nominal pulse-length of 34 ns. All laser micromachined samples consisted of a 400 µm diameter circular pit of depth ca. 5 µm, machined into the growth face. Machining parameters were set at a pulse frequency of 100 Hz i.e. one ns-pulse per 0.01 s, with a fluence of 15 J cm^{-2}, at a speed of 0.3 mm s^{-1}; parameters typical of those used in the laser micromachining of BDD electrodes.[33,35] For electrochemical tests, the pits were machined in quintuplicate (×5), and spaced such that they were individually addressable. For electrochemical studies it was necessary to produce a reliable titanium carbide ohmic contact to the BDD. Ti (10 nm) / Au (400 nm) was sputtered (MiniLab 060 Platform sputter/evaporator, Moorfield Nanotechnology) onto the back face of the laser micromachined BDD electrodes and the electrode annealed at 400 °C for 5 hours.[47]

Oxidative Acid Treatment: BDD laser machined electrodes were acid oxidised at ~200 °C, in concentrated H_2SO_4 (98%) saturated with potassium nitrate (KNO_3) for a time of 30 minutes; equating to exhaustion of all the KNO_3 in solution. Adding the KNO_3 to sulphuric acid to create nitric acid *in-situ*, generates a more oxidising environment, than sulphuric acid alone. For time dependent experiments, acid oxidation times of 15 minutes, 2 hours and 24 hours were also employed (**ESI 1**), using the same solution. Finally, measurements were also made using solutions which had the exhausted KNO_3 refreshed every 30 mins (up to n=4 treatments).

Thermal Oxidation Treatment: BDD laser machined electrodes were thermally oxidised in air, in a tube furnace oven, (Thermo, Lindberg Blue/M) at temperatures over the range 400 °C to 600 °C for 5 hours each. For a fixed temperature of 600 ºC, the thermal oxidation time was also varied between 15 minutes to 5 hours.

Electrochemical setup

All electrochemical measurements were performed using a three-electrode configuration, with platinum and a saturated calomel electrode (SCE) electrode utilised as counter and reference electrodes respectively. ns-laser micromachined BDD electrodes for electrochemical characterisation were mounted onto a Ti/Au sputtered glass slide using silver epoxy (RS Components Ltd.). In order to restrict the electrode area, Kapton tape (RS Components Ltd.) containing 1 mm diameter holes was positioned to electrochemically isolate one of the five pits. This isolated area was used as the working electrode and repeated for all five pits in a similar manner. Once secured the Kapton mask was kept in place to ensure the electrode surface was not contaminated. ns-laser micromachined cylinder electrodes consisted of a 1 mm BDD diameter cylinder sealed in a glass capillary, the fabrication of which has been described previously.[6] All potentials are quoted versus SCE. Solvent window measurements are calculated using a current density threshold of ±0.4 mA cm^{-2}, used previously to assess BDD film quality.[45] Γ measurements were performed as previously described.[21]

White Light Laser Interferometry (WLI)

A Bruker ContourGT (Bruker Nano Inc., USA) was used to record WLI profiles. 3D rendering of interferometry data was performed and the total electrode area and surface roughness calculated after machining using Gwyddion 2.42.[48]

Transmission Electron Microscopy

Single TEM lamellae (electron transparent region dimensions typically 5 µm × 3 µm × 100 nm: length × height × thickness) were cut using standard Focused Ion Beam (FIB) lift-out procedures on an FEI Scios DualBeam FIB Microscope. To prevent any damage to the surface, which could be mistaken as a result of the electrode processing stages, surface layers of Pt were deposited on the surface prior to FIB milling. The Pt was ion beam deposited, unless when depositing directly onto the diamond/sp^2 bonded carbon interface. Here a thin layer of electron beam deposited Pt was put down first. Lamellae were also prepared from fresh, separate, electrodes for each stage of the processing to ensure that any change in observed microstructure were solely the result of the processing and not due to damage from previous TEM lamella preparation. For the oxidatively-treated samples, an additional layer of aluminium (from 20 nm to several hundred nm's) was sputtered/evaporated onto the surface (MiniLab 060 Platform sputter/evaporator, Moorfield Nanotechnology) prior to Pt deposition. The application of the Al layer was two-fold, first to act as an additional layer to protect the surface from damage during the FIB process and secondly separating the BDD surface from the deposited Pt layer. Pt layers deposited in the FIB typically contain a high carbon content from the breakdown of the Pt precursor gas[49]. The presence of an sp^2 bonded carbon signature in the Pt complicates the mapping of sp^2 bonded carbon by EELS and may provide misleading information. A schematic of the different FIB lamellae prepared for the studies described in the main text is shown in Figure 1.

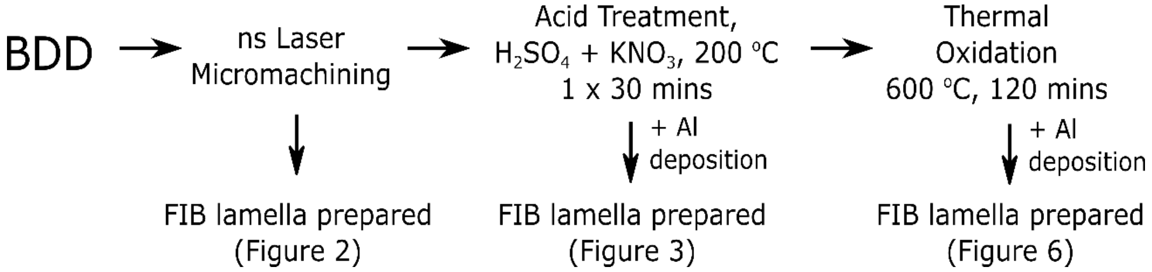

Figure 1: Schematic showing the different lamallae processing routes for the BDD electrodes.

The cross-section specimens were examined using conventional TEM in a JEOL 2100 LaB_6 and scanning TEM (STEM) using a double-aberration corrected JEOL ARM200F (Schotttky FEG) equipped with a Gatan Quantum EELS Spectrometer, at an accelerating voltage of 200kV. Samples were tilted so that the electron beam lay parallel to the interface between the regions of interest to minimise projection effects. Standard Spectrum Imaging (SI) methodology[50] was utilised for EELS data acquisition with a convergence angle of 16 mrad and a collection semi-angle of 25 mrad. Background subtraction, deconvolution, and subsequent analysis was carried out using standard routines found in Gatan's Digital Micrograph software. High Angle Annular Dark Field (HAADF) and (Medium Angle - MA) ADF imaging was carried out at the same time as the EELS mapping. Both ADF and HAADF imaging detects electrons which have been scattered from the optical axis and as such both techniques are sensitive to atomic number (often called Z-contrast). However, HAADF imaging detects electrons which have been scattered to larger angles than ADF imaging. This makes HAADF more sensitive to Z-contrast and less susceptible to other mechanisms which can contribute to image contrast, such as diffraction.

Results and Discussion

Understanding the Structure of Laser Micromachined BDD

ns-laser micromachining only

Figure 2a shows the BDD surface after ns-laser micromachining, in cross section imaged using the HAADF detector. The grain size of the polycrystalline BDD material (10's of µm) is much larger than the lamella size (in fact, no BDD grain boundaries were present in any of the lamella imaged). Several layers can be identified and are labelled in Figure 2a. At the bottom of the image is the BDD, and at the top of the image is the protective Pt layer (here a thin layer of . Sandwiched between the two is non-BDD material up to 1 µm thick. Two layers are visible in this material, labelled I and II, although the interface between them is not clearly defined. The HAADF contrast difference between the BDD, and layers I and II, is a result of the material being less dense than the BDD, hence less scattering to larger angles, rather than Z-number (as both regions only contain carbon and trace boron). This is in contrast to the case for Pt where the higher Z number results in the brighter contrast. Layer II is also deeply fissured, made clear by penetration of the Pt through this layer.

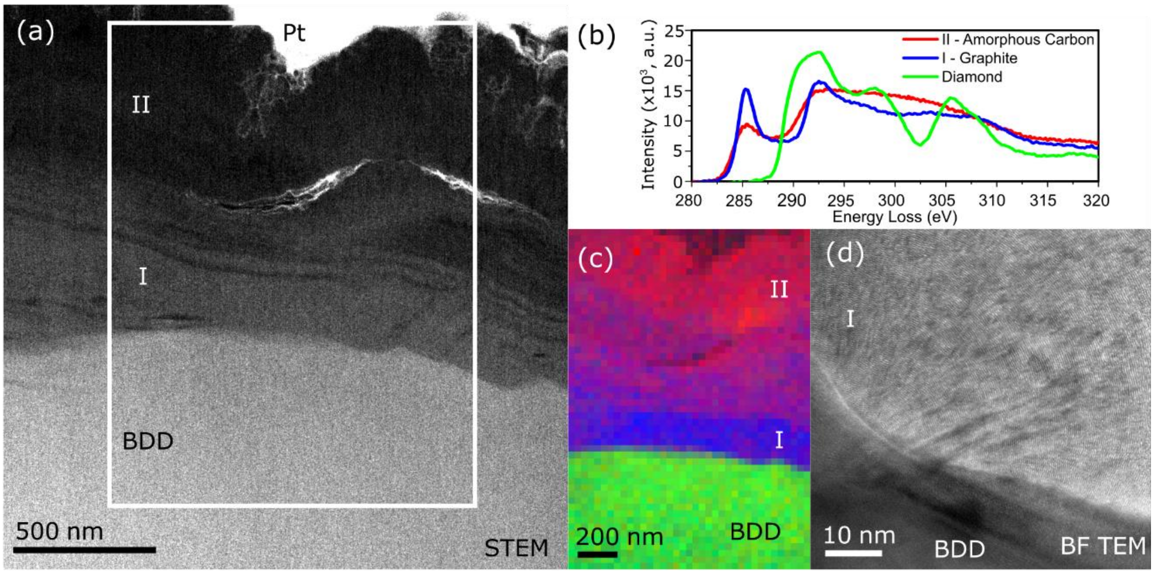

Figure 2: (a) HAADF STEM image with white rectangle indicating EELS survey area b) EELS spectra of BDD (green), graphite (blue) and amorphous carbon (red), obtained from the BDD substrate, layers I and II respectively. Spectra have been scaled to fit the axis (c) Multilinear Least Squares fitting of the 3 spectra in (b), showing the distribution of BDD, graphite and amorphous carbon. (d) High magnifcation BF TEM image confirming that layer I is composed of graphite, in agreement with the EELS analysis.

EELS SI was used to map the sp^2/sp^3 bonded carbon character of the three regions over the area defined by the white box in Figure 2a. Averaged EELS spectra from the BDD (green line), layer I (blue line) and layer II (red line) can be seen in Figure 2b, and are found to be consistent with the spectra of diamond, graphite and amorphous carbon respectively[51]. The sp^2 character of the graphite (layer I) and amorphous carbon (layer II) is evident by the peak in the EELS spectra at 285 eV, caused by a $1s \rightarrow \pi^*$ transition [52,53], a transition only seen in sp^2 bonded carbon. The differences in the fine structure of the carbon K-edge (seen within 50 eV of the edge onset) between diamond, graphite and amorphous carbon provides information about the local density of states which reflects the differences in the local bonding configuration[54].

To map out the spatial distribution of the diamond, graphite and amorphous carbon at the laser ablated surface, Multi Linear Least Squares (MLLS) fitting of the EELS spectrum image has been carried out on the region marked in Figure 2a using Gatan Digital Micrograph software**.** For each pixel in the spectrum image, the spectrum was fitted using a linear combination of the diamond, graphite and amorphous carbon spectra seen in Figure 2b. The fit coefficients for each of the three component spectra from the MLLS fit have been plotted in a colour map,

Figure 2c, and show how each of the different carbon phases is distributed (crystalline BDD - green, crystalline graphite – blue, and amorphous carbon - red).

Figure 2c shows that an approx. 200 nm thick layer of almost pure graphite can be seen directly on top of the BDD, attributed to the ns-laser induced solid-solid phase transition of BDD to graphite. Bright field (BF) TEM imaging shows that layer I exhibits lattice fringes with a spacing of 0.34 nm (as expected for graphite), Figure 2d, confirming the results of the EELS analysis. A larger version of Figure 2d is presented in ESI 1 to enable the graphitic fringes to be seen more easily. Close to the interface either parallel or perpendicular graphite orientations are observed. In some areas, both parallel and perpendicular orientations are present, as a result of curving of the perpendicular planes, Figure 2d. Away from the interface the graphite is orientated at predominantly ~ 45^o to the BDD over large areas (100’s nm) suggesting that crystallization occurs over relatively long timescales, much longer than individual ns laser pulses. We see no preferential crystallographic orientation for the BDD. Moving up to layer II, Figure 2c indicates a gradual change from graphite to amorphous carbon over several hundred nm. The MLLS fit indicates that the upper section of layer II is primarily amorphous in nature, also in agreement with TEM imaging (not shown). Layer II is likely to result from re-deposition of carbon from the plasma phase, due to sublimation or vaporization of the graphitic material [9]. The composition of the damage layer formed in this highly doped BDD, is thus very similar to that produced in diamond when subject to ns-laser micromachining, suggesting the mechanism is independent of boron concentration.[9]

ns-laser micromachining followed by oxidative acid treatment

The effect of an acid oxidative treatment on the laser induced layers I and II was examined. Figure 3a shows an ADF STEM image of a cross-section of the ns laser cut BDD after sulfuric acid oxidation for 30 minutes at elevated temperature (200 ^oC) in the presence of KNO_3. 30 mins is typically the time taken for exhaustion of all of the KNO_3. Note, this sample contains a protective Al/Pt layer. In contrast to the ns laser micromachined only sample, a significantly thinner continuous dark layer with varying thickness can be seen between the BDD and Al. This dark layer appears to be composed of clusters of a thicker material (up to 40 nm) connected by thin layers (~5 - 8 nm) on the BDD surface. MLLS fitting of the EELS spectrum image (Figure 3a inset) using the spectra from Figure 2b shows the clusters are comprised primarily of graphite; the averaged spectra obtained for the cluster (Figure 3b, blue) is similar to that obtained from layer I (Figure 2b, blue). TEM imaging of these clusters also confirm them to be highly oriented graphite, Figure 3c. In all the observed clusters, interestingly, the graphite is found with its basal plane perpendicular to the BDD surface, Figure 3c and d. This suggests the survivability of the graphite could be dependent on its orientation to the underlying BDD.

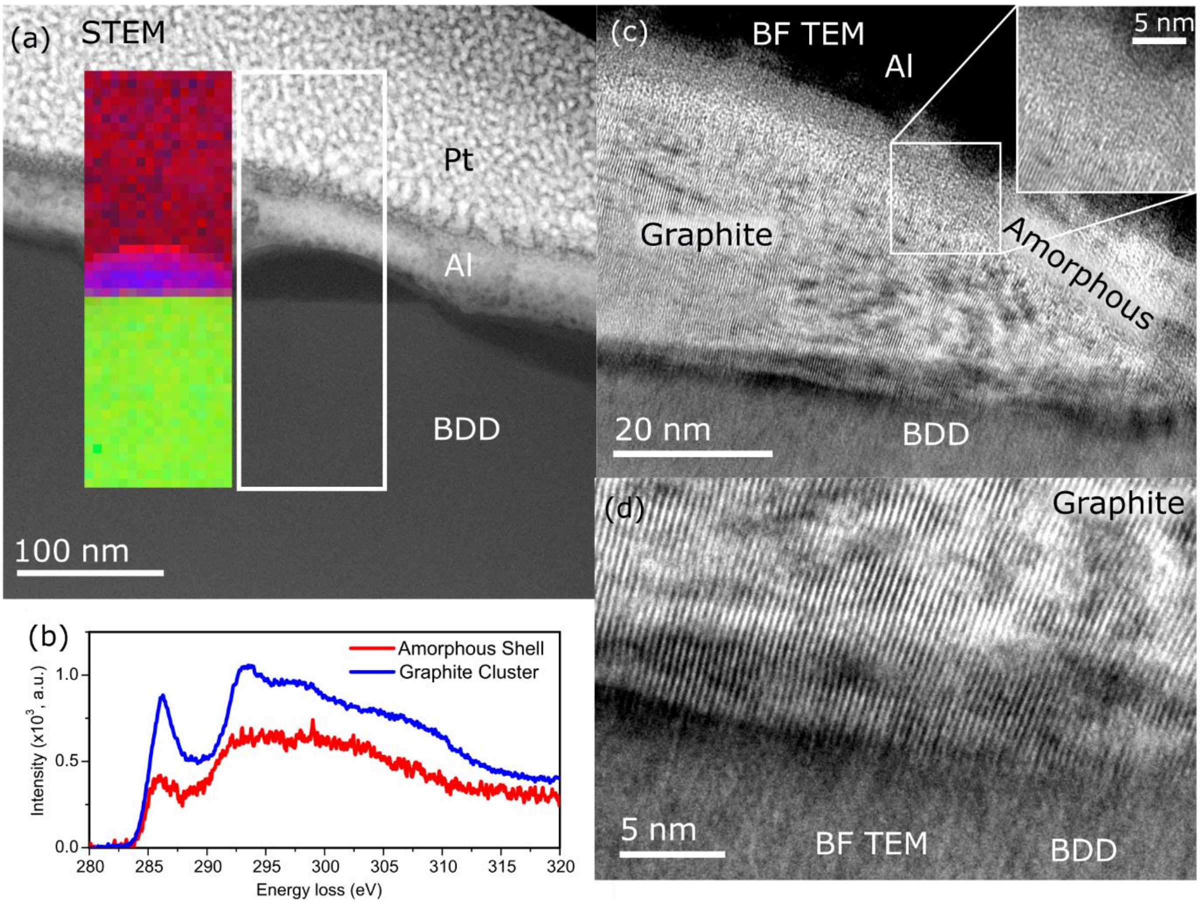

Figure 3: (a) HAADF STEM image of ns laser micromachined BDD after acid cleaning, Inset: shows the MLLS fit using the diamond, graphite and amorphous carbon spectrum. (b) EELS spectrum obtained from the graphite cluster (blue) and the spectrum from the amorphous shell (red). Spectra rescaled to plot on same axis. (c) High resolution TEM image showing the graphite cluster with basal planes perpendicular to BDD interface and a thin amorphous top layer. Inset shows the amorphous shell-graphite interface. d) BF-TEM image showing the graphite-BDD interface.

Comparing this layer and layers I/II prior to the acid oxidation (Figure 2), it is clear that all of the amorphous (and fissured) carbon (layer II) has now been completely removed and that the clusters are remnants of graphite (layer I) that have survived the oxidative acid treatment. Importantly, these perpendicularly orientated graphite clusters appear to be encapsulated by an amorphous carbon shell approximately 5 nm in thickness (Figure 3c inset); also shown by the increase in the fit coefficient of the amorphous carbon signal directly adjacent to the graphite signal in the MLLS fit (Figure 3a inset). The amorphous character of the shell (Figure 3b, red) can be clearly seen in comparison to the graphite (Figure 3b, blue), and with comparison to the EELS spectrum of layer II in the laser ablated sample (Figure 2b, red). We speculate that this amorphous shell forms as a result of the acid oxidative etch of the graphite (layer I) and is the reason why these graphite clusters withstand complete removal by the acid treatment. To differentiate this amorphous layer from the amorphous, fissured carbon of layer II (Figure 2), which does etch easily in acid, we term this material "denatured graphite". From the EELS spectra, the sp^2 bonded carbon fraction of this region was determined using the method described by Bruley *et al* [55,56]. Using the graphite layer (I) from the ns laser micromachined sample (Figure 2) as 100% sp^2 reference material, the sp^2 bonded carbon fraction of this encapsulating amorphous shell was found to be approx. 70% sp^2 bonded carbon. Note, in the thin layers between the clusters, TEM imaging was not able to resolve any planes of graphite and the EELS analysis was inconclusive as to the nature of this material. As such we speculate this is also "denatured graphite".

It is important to note, whilst the majority of the remnant clusters are composed of perpendicular-orientated graphite, it is the encapsulating amorphous shell, and not the graphite itself, which interfaces with the electrolyte solution. This surface also plays host to the many different oxygen functional groups, such as quinones, across which electrochemical electron transfer takes places. Tracking of the electrochemical quinone surface coverage response[21] enables the sp^2 bonded carbon surface content to be correlated with subsequent acid treatments. For example, as shown in ESI2, even by acid oxidizing for significantly longer periods of time, in the same solution (24 hours), or by refreshing the KNO_3 concentration in the acid solution every 30 mins (over an n=4 cycle), the quinone response stays relatively stable. This is also indicative of incomplete removal of the sp^2 bonded carbon layer from the surface of the BDD. TEM analysis of the effect on the ns laser micromachined BDD surface of a second addition of KNO_3 to the acid solution, is described in ESI3. Briefly, ESI3 shows that the graphite clusters remain on the BDD surface, supporting the electrochemical data. Whilst the robustness of this remaining layer towards complete removal by acid oxidation is somewhat surprising, it is also extremely useful for electrochemical applications which make use of this hybrid sp^2-sp^3 bonded material,[13,33,35] especially in the more challenging solution environments.[38]

Thermal oxidation of laser ablated BDD

Thermal oxidation was next investigated as a means for sp^2 removal from the ns-laser micromachined BDD surface. 30 min acid oxidized surfaces were employed for all these studies, which from Figure 3, contain perpendicularly orientated clusters of graphite capped by a layer of "denatured graphite". Removal of sp^2 bonded carbon, was first investigated using electrochemical quinone Γ measurements, for a fixed thermal oxidation time (= 5 hrs) and temperatures of 400, 465, 500, 550 and 600 °C. As shown in Figure 4, as the temperature of oxidation is increased a reduction in Γ is evident, to non-detectable levels at a temperature of 600 °C after 5 hrs. Higher temperatures were not investigated to limit damage to the remaining sp^3 material, with rapid graphitisation reported at 700 °C in air.[57]

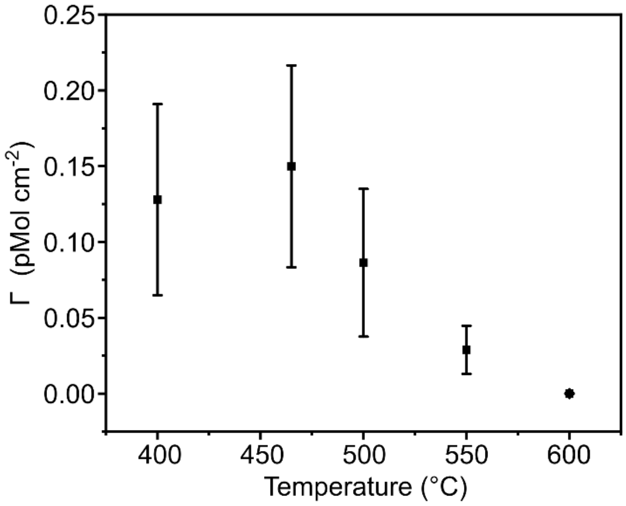

Figure 4: Effect of thermal oxidation temperature on Γ

At temperatures in the range 400 °C to 465 °C, no statistically significant change in the surface coverage of surface integrated quinones was seen. Interestingly, this is contrary to the work of Osswald et al. [31] that reported sp^2 bonded carbon can be removed from the surface of nanodiamonds with temperatures as low as 425 °C in air. This suggests that the sp^2 bonded carbon coating on a nanodiamond, which consists of carbon onions, graphite ribbons, amorphous carbon and fullerenic shells [31] is less thermally stable than that found on the BDD surface after ns-laser machining. This may be due to the presence of the "denatured graphite" layer. For nanocrystalline diamond which contains a high content of sp^2 bonded carbon residing in grain boundaries, thermal treatment at 550 °C in air, was shown to partially remove the non-diamond-phase, resulting in pore formation.[58]

As 600 °C was shown to remove all electrochemically active sp^2 bonded carbon material after 5 hrs (denoted on Figure 4 as $\Gamma = 0 \pm 1.7 \times 10^{-16}$ mol cm^{-2}, the uncertainty being the limit of detection[21]), the effect of thermal oxidation time was investigated for a fixed temperature of 600 °C. As shown in Figure 5a, quinone Γ undergoes an exponential decay with time. The natural logarithm can be plotted to extract a first order thermal oxidation rate constant (Figure 5b), with respect to quinone surface coverage, yielding a value of -0.02761 min^{-1}. Using electrochemical measurements, within the limit of quinone detection, all measurable material sp^2 bonded carbon content was removed after 2 hours. Rate constants calculated at the different temperatures enabled construction of an Arrhenius plot (**Figure 5c**), and the calculation of an activation energy of 130 kJ mol^{-1}, which is on the expected order of C-C bond breaking.[59]

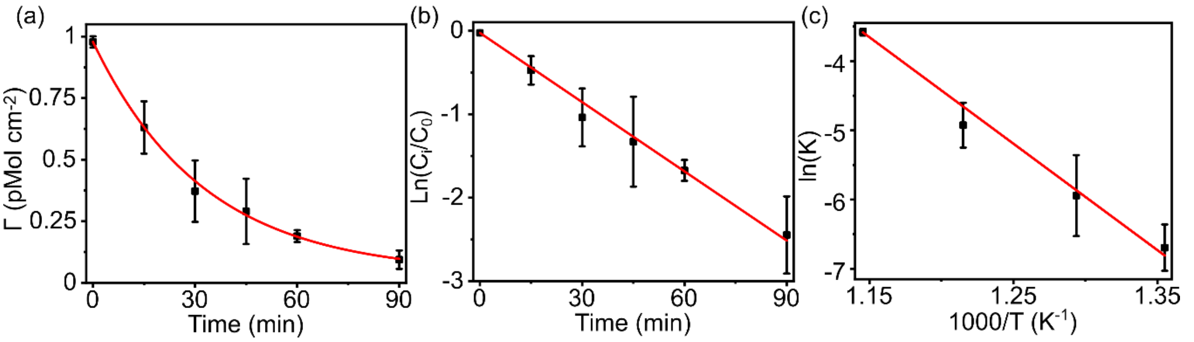

Figure 5: (a) Exponential decay of Γ upon thermal oxidation at 600°C, which can be used to infer on the removal of surface sp^2 (b) first order dependence of Γ on time (c) Arrhenius plot

High resolution TEM was employed to microscopically investigate the material after 2 hrs thermal oxidation at 600 °C in air. Figure 6a shows an ADF STEM image of a cross section of the ns-laser ablated BDD, after treatment. An evaporated Al layer was added to encapsulate the surface, after thermal oxidation. As with Figure S2, a layer of gold contamination is observed at the interface (ESI2), this layer does not affect the results of the EELS SI although the bright intensity of the Au does obscure the interface from being seen in ADF and HAADF STEM imaging. No clusters of graphite were observed after the thermal oxidation process. A small increase in the sp^2 bonded carbon signal, the 1s → π* transition at 285eV, was observed in the EELS spectrum at the interface, although of importance, the total integrated sp^2 signal was significantly decreased compared to the ns laser micromachined sample and those samples subject to further acid treatments. The sp^2 bonded carbon fraction over a distance of 32 nm from within the BDD up to the Al layer, was calculated from the EELS spectra (Figure 6b).

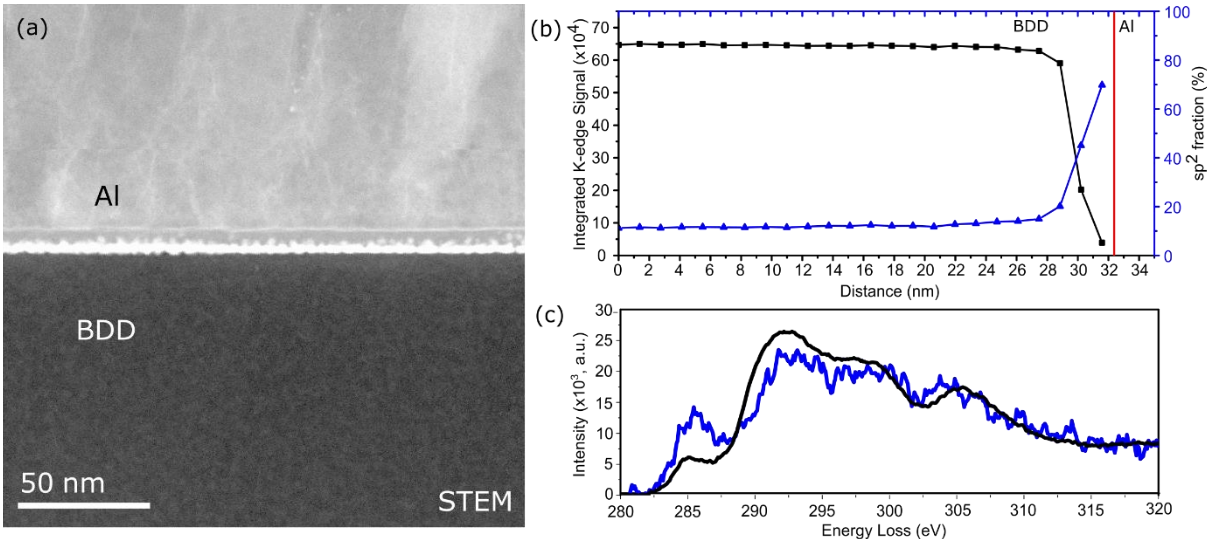

Figure 6: (a) ADF STEM image of the interface between thermally oxidized BDD and the Al protecting layer. The BDD was first ns laser micromachined then subject to an acid oxidative treatment. The bright layer is Au contamination from the Al protection process. No large clusters of graphite are observed on the BDD surface. (b) Plot showing the sp^2 fraction of the material and the integrated carbon K-edge signal between 280-340 eV approaching the interface with Al (indicated by the vertical red line). (c) EELS spectra from the 1st (blue) and 2nd (black) pixels before the solid vertical red line. Spectra have been scaled to fit the axis.

The sp^2 bonded carbon fraction (of approx. 10%) within the BDD (**Figure 6b**) is most likely FIB-induced damage at the surface of the lamella during TEM specimen preparation and is similar to values found in the previous samples. EELS shows an increase in the sp^2 fraction (above background contamination levels) close to the interface along with a corresponding decrease in the integrated carbon K-edge signal (Figure 6b), which could be indicative of a thin layer (<3 nm) of surface contaminants. Regardless of surface termination, hydrocarbons, H_2O, etc. are readily absorbed onto the diamond surface upon exposure to atmosphere[60,61]. The solid red vertical line denotes the edge of the Al layer, where the carbon K-edge signal decreases to zero. The EELS spectrum of the point ~3 nm to the left of the solid red vertical line (Figure 6b) retains many of the features seen in the diamond spectrum, Figure 6c (black), with the addition of the pre-edge sp^2 peak. The pixel size of 1.4 nm is likely larger than the surface roughness therefore energy losses from both the diamond and surface contaminants are being detected leading to the 45% sp^2 fraction measured. Close to the Al layer the carbon K-edge signal decreases dramatically and the spectrum is close to that of amorphous carbon, Figure 6c blue, with an sp^2 fraction of 70% being measured. Note, the thickness over which this sp^2 bonded carbon signal can be seen at the interface may be an effect of the tilt being slightly off-parallel to the interface, and the contamination layer may occur over a depth less than 3 nm from the surface.

To complement the electrochemical quinone measurements, which gave undetectable signals after 2 hrs thermal treatment at 600 ^{o}C, the solvent window of this electrode material, in the electrolyte 0.1 M KNO_3, increased significantly from +1.7 to +3.3 V using a current threshold of 0.4 mA cm^{-2}. This is due to a decrease in the electrocatalytic activity of the electrode towards water reduction. Values >3 V are typically associated with minimal sp^2 content BDD.[3,45] The TEM and electrochemical data together suggest removal of electrocatalytically active sp^2 bonded carbon, important for any electrochemical application which requires a sp^2 bonded carbon free electrode. Note, based on our data, we recommend, with ns laser micromachined material, performing the acid oxidative treatment first to significantly reduce the layer of sp^2 bonded carbon on the surface, with thermal oxidation being used to remove the remaining small clusters which acid oxidation leaves behind. Given the μm scale thickness of the sp^2 bonded carbon layer (Figure 2), and thermal etch rates reported, significantly long thermal oxidation times are envisaged using the thermal oxidation method alone.

The studies described herein on the differently treated BDD materials allow us to postulate the following steps for the removal of non-diamond damaged material from ns laser micromachined BDD, Figure 7. During oxidative acid treatment, all of the amorphous carbon layer II is removed to leave behind a greatly modified layer I, containing clusters of perpendicularly orientated graphite capped with a layer of amorphous “denatured graphite” carbon which cannot be removed by longer or multiple acid treatments. However, a 600 ^{o}C thermal oxidation treatment is able to remove the majority of this material to leave a surface with significantly improved electrochemical performance, associated with the loss of sp^2 bonded carbon.

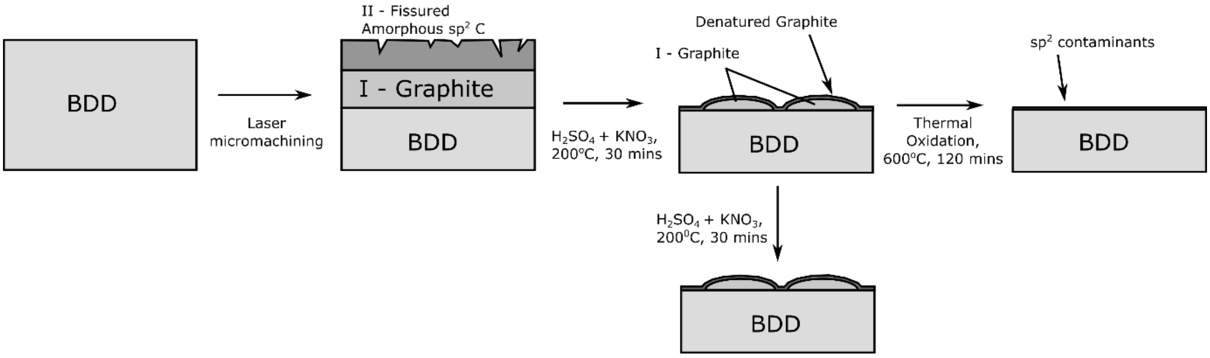

Figure 7: Schematic showing BDD processing and layers identified from TEM imaging of FIB lamellae produced at each stage. Not to scale.

Application to laser micromachined BDD cylinders

The ns laser micromachining of BDD cylinders or “rounds” which are then sealed in an insulator e.g. glass capillaries, is a common fabrication method for forming easy-to-handle BDD disk electrodes.[6] However, due to the sp^2 bonded carbon creation, co-planar glass-sealed BDD rounds will also contain a ring of sp^2 bonded carbon. The situation is exacerbated if the BDD cylinder protrudes from the glass surround. If unaccounted for this will lead to incorrect values being ascribed to the electron transfer kinetics of electroactive analytes at BDD.[20]

To investigate the effectiveness of the thermal oxidation process at removing sp^2 bonded carbon from the sidewall of ns laser micromachined rounds, BDD thermally oxidized cylinders (5 hrs at 600^{o}C) were sealed in glass and polished flat. The electrochemical characteristics of the BDD electrode, in particular Γ, solvent window and electrochemical double layer capacitance (C_{dl}), were compared against those values recorded for BDD electrodes defined by use of an insulating Kapton mask on a planar BDD surface. This method removes all laser cut edge effects.[21] In both cases the electrode material was the same. Similar values were recorded for all three parameters, in particular Γ was undetectable for both, the solvent window was 3.7 ± 0.12 V (cylinder) versus 3.71 ±0.04 (Kapton mask) and C_{dl} was 4.2 ± 0.2 $\mu F\ cm^{-2}$ (cylinder) versus 3.9 ± 0.2 $\mu F\ cm^{-2}$ (Kapton mask).

For quantitative electrochemical analysis the area of the electrode and surface roughness are important parameters to know to aid in quantification of electrochemical data. To this regard, whilst the treatment is effective at removing cylinder sidewall sp^2 bonded carbon, it is important to also assess the impact of thermal oxidation on the resulting surface roughness of the electrode face. Minimal sp^2 bonded carbon and polished BDD, with an initial surface roughness of 1.11 ± 0.07 nm, was oxidized at 600 ^{o}C in air for times in the range 30 minutes to 5 hours The resulting surface roughness was measured using WLI, over an area of the surface typically 12 × 9 µm. As Figure 8a shows increased thermal oxidation time leads to an increasing surface roughness, increasing linearly at 8 nm $hour^{-1}$ from 1.11 ± 0.07 nm to 41 ± 1 nm RMS over 5 hours, also suggesting etching of the sp^3 carbon material. However, while the relative increase in roughness is significant ($p<0.05$), the absolute change in roughness and surface area is low and is only measurable due to the very low surface roughness of the starting polished surface (Figure 8b, inset).

From WLI recorded on the polished BDD surface before (inset, Figure 9b) and after 5 hrs thermal oxidation at 600 ^{o}C (Figure 8b) it was apparent that the main roughness component was due to both grain boundary etching, where the largest changes in height were observed, and differential thermal oxidation rates on different grains. The former suggests it is the more highly strained, defective sp^3 bonds on the grain boundaries that are etched preferentially, assuming minimal sp^2 bonded carbon presence.[62,63] The on-grain roughness after 5 hrs treatment was recorded as 3.3 ± 0.3 nm (n= 20) (total = 41 ± 1 nm RMS).

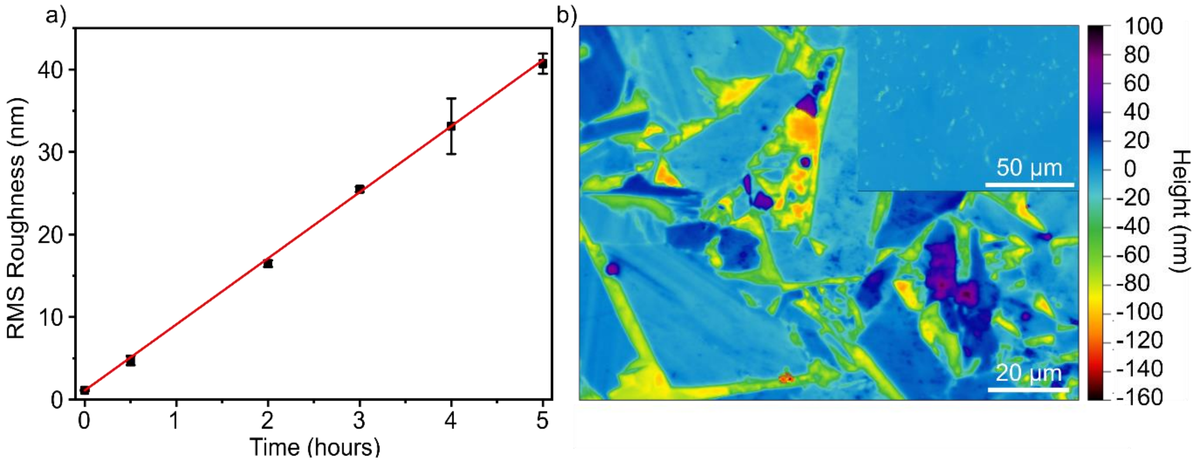

Figure 8: (a) Surface roughness (RMS) dependence on time and (b) WLI image of a mechanically polished and acid oxidatively cleaned, minimal sp^2 bonded carbon content BDD surface after 5 hours thermal oxidation, demonstrating the different etching rates on different grains and on grain boundaries. inset: WLI image of surface after 0 hours of thermal oxidation, same Z scale.

Application to as grown sp^2 containing BDD

Whilst the data shows that thermal oxidation can be used to remove sidewall sp^2 bonded carbon from ns micromachined laser cut cylinders of BDD, it is interesting to consider whether the method can also be employed to remove sp^2 surface bonded carbon present as a result of the CVD growth process. The electrochemical characteristics of thin film microcrystalline BDD, grown via hot filament CVD and thus more susceptible to sp^2 bonded carbon inclusion compared to microwave CVD,[64] was thermally oxidized at 600 ^{o}C in air for 2 hrs. Electrochemical properties before and after treatment were compared. The solvent window in aqueous solution improved markedly, increasing from 2.5 ± 0.4 V to 3.21 ± 0.06 V,(Figure 9a) due to the removal of sp^2 bonded carbon that is more catalytically active towards water oxidation and reduction.[65] Γ also decreased by over two orders of magnitude from 1.8 ± 0.3 pmol cm^{-2} to 5 ± 1 fmol cm^{-2} (close to the limit of detection: 1.6 fmol cm^{-2} [21], Figure 9b). Note, the starting Γ values here are almost double that of Figure 5a and after 5 hours there was no detectable Γ signal. The electrode to electrode variation in solvent window also reduced following thermal oxidation. This is likely to be due to heterogeneities in the amount and form of sp^2 bonded carbon present per electrode. Using as-grown thin film microcrystalline material (starting RMS roughness = 1.1 µm, much higher than the polished material) no measurable increase in roughness was observable after 5 hrs thermal treatment.

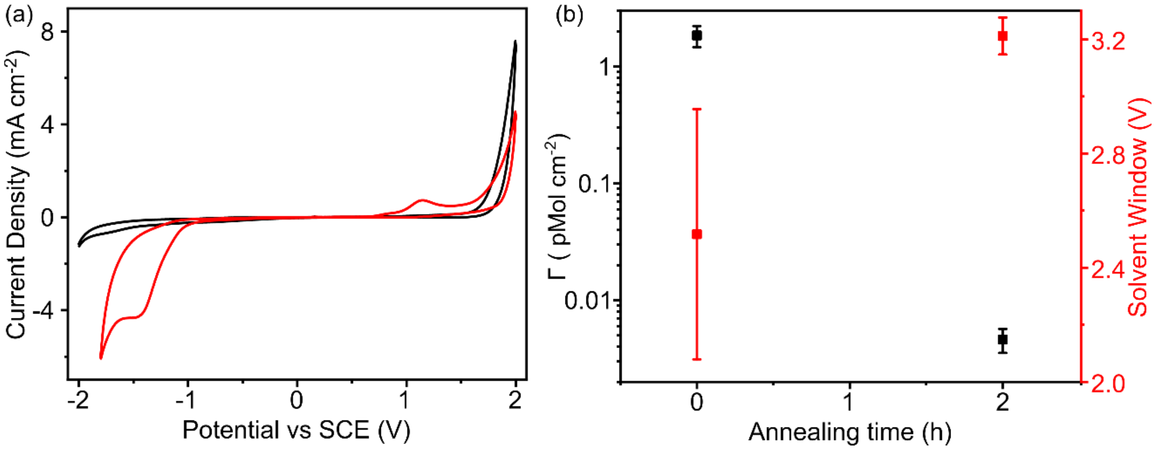

Figure 9: (a) Cyclic voltammograms in KNO_3 showing the solvent window before (red) and after (black) thermal oxidation for 2 hrs at 600°C (b) Γ (black) and solvent window (red) before and after thermal oxidation, showing the improvement in these metrics of electrochemical performance

Conclusions

Methods to remove sp^2 bonded carbon from the surface of BDD, created either as a result of material processing or growth have been investigated by both TEM and electrochemical techniques, the latter inherently surface sensitive. ns laser micromachining of BDD, commonly used to cut and structure diamond/BDD, is shown to result in surface damage, and the formation of a ~µm thick coating of sp^2 bonded carbon. This coating contains a layer of highly ordered graphite intimately attached to the BDD, which transitions to a layer of fissured amorphous carbon. Similar structures have been seen on ns laser micromachined diamond. [9] Oxidative acid treatment (sulfuric acid and potassium nitrate) at elevated temperature, a common cleaning recipe for diamond/BDD, is shown to be ineffective at removing all the sp^2 bonded carbon. Whilst the fissured amorphous layer and parallel-orientated graphite regions are removed completely, the perpendicular orientated graphitic regions (10's nm in diameter) remain. These are considerably thinner in size and capped with a ~5 nm thick layer of amorphous carbon, we term "denatured graphite". Further oxidative acid treatments still cannot remove these clusters, which we speculate is due to the formation of this cap layer during the first acid etch. However, cluster removal is possible via thermal oxidation in air at 600 °C. TEM detects a very thin (~ nm) layer of sp^2 bonded carbon at the interface, but this is likely to be due to surface contamination. The electrochemical response (solvent window, double layer capacitance, quinone coverage) of this surface closely resembles that of a minimal sp^2 bonded carbon content BDD electrode.

Finally, the versatility and simplicity of the thermal oxidation process in removing sp^2 bonded carbon was demonstrated electrochemically on both ns laser micromachined BDD cylinders and hot filament CVD grown BDD films containing surface sp^2 bonded carbon. Thermal oxidation in air can be performed with equipment available in the majority of laboratories. As such it offers a convenient method for users to improve the material properties of intrinsic and doped diamond materials after growth or processing for a wide range of applications where the presence of sp^2 carbon is detrimental to material performance.

Acknowledgements

The authors would like to acknowledge the Warwick Electron Microscopy Research Technology Platform and the WMG Advanced Manufacturing and Materials Centre at the University of Warwick for use of their electron microscopes. We acknowledge the Centre for Doctoral Training in Diamond Science and Technology (EP/L015315/1) (SJC, FHJL, GW) with the Defence Science and Technology Laboratory (Dstl) (SJC) and De Beers (FHJL). We acknowledge the Royal Society for an Industry Fellowship (JVM, INF/R1/180026). We thank Element Six Ltd. for supplying BDD material.

Appendix A. Supplementary data

Supplementary data to this article can be found online at:

References

[1] S.J. Cobb, Z.J. Ayres, J. V. Macpherson, Boron Doped Diamond: A Designer Electrode Material for the Twenty-First Century, Annu. Rev. Anal. Chem. 11 (2018) annurev-anchem-061417-010107. https://doi.org/10.1146/annurev-anchem-061417-010107.

[2] N. Yang, S. Yu, J. V. Macpherson, Y. Einaga, H. Zhao, G. Zhao, G.M. Swain, X. Jiang, Conductive diamond: synthesis, properties, and electrochemical applications, Chem. Soc. Rev. 48 (2019) 157–204. https://doi.org/10.1039/C7CS00757D.

[3] J. V Macpherson, A practical guide to using boron doped diamond in electrochemical research., Phys. Chem. Chem. Phys. 17 (2015) 2935–49. https://doi.org/10.1039/c4cp04022h.

[4] N. Yang, J. Hees, C.E. Nebel, Diamond Ultramicro- and Nano-electrode Arrays, in: N. Yang (Ed.), Nov. Asp. Diam. From Growth to Appl., Springer International Publishing, Cham, 2015: pp. 273–293. https://doi.org/10.1007/978-3-319-09834-0_9.

[5] L.A. Hutton, M.E. Newton, P.R. Unwin, J. V Macpherson, Factors Controlling Stripping

Voltammetry of Lead at Polycrystalline Boron Doped Diamond Electrodes: New Insights from High-Resolution Microscopy, Anal. Chem. 83 (2011) 735–745. https://doi.org/10.1021/ac101626s.

[6] L. Hutton, M.E. Newton, P.R. Unwin, J. V Macpherson, Amperometric Oxygen Sensor Based on a Platinum Nanoparticle- Modified Polycrystalline Boron Doped Diamond Disk Electrode Amperometric Oxygen Sensor Based on a Platinum Nanoparticle-Modified Polycrystalline Boron Doped Diamond Disk Electrode, Anal. Chem. 81 (2009) 1023–1032. https://doi.org/10.1021/ac8020906.

[7] M. Pagels, C.E. Hall, N.S. Lawrence, A. Meredith, T.G.J. Jones, H.P. Godfried, C.S.J. Pickles, J. Wilman, C.E. Banks, R.G. Compton, L. Jiang, All-diamond microelectrode array device, Anal. Chem. 77 (2005) 3705–3708. https://doi.org/10.1021/ac0502100.

[8] C. Batchelor-McAuley, C.E. Banks, A.O. Simm, T.G.J. Jones, R.G. Compton, The electroanalytical detection of hydrazine: A comparison of the use of palladium nanoparticles supported on boron-doped diamond and palladium plated BDD microdisc array, Analyst. 131 (2006) 106–110. https://doi.org/10.1039/B513751A.

[9] P.W. Butler-Smith, D.A. Axinte, M. Pacella, M.W. Fay, Micro/nanometric investigations of the effects of laser ablation in the generation of micro-tools from solid CVD diamond structures, J. Mater. Process. Technol. 213 (2013) 194–200. https://doi.org/10.1016/j.jmatprotec.2012.08.010.

[10] K. Arihara, C. Terashima, A. Fujishima, Electrochemical Production of High-Concentration Ozone-Water Using Freestanding Perforated Diamond Electrodes, J. Electrochem. Soc. 154 (2007) E71. https://doi.org/10.1149/1.2509385.

[11] R. Hoffmann, A. Kriele, H. Obloh, J. Hees, M. Wolfer, W. Smirnov, N. Yang, C.E. Nebel, Electrochemical hydrogen termination of boron-doped diamond, Appl. Phys. Lett. 97 (2010). https://doi.org/10.1063/1.3476346.

[12] S. Odake, H. Ohfuji, T. Okuchi, H. Kagi, H. Sumiya, T. Irifune, Pulsed laser processing of nano-polycrystalline diamond: A comparative study with single crystal diamond, Diam. Relat. Mater. 18 (2009) 877–880. https://doi.org/10.1016/j.diamond.2008.10.066.

[13] Z.J. Ayres, A.J. Borrill, J.C. Newland, M.E. Newton, J. V. Macpherson, Controlled sp2 Functionalization of Boron Doped Diamond as a Route for the Fabrication of Robust

and Nernstian pH Electrodes, Anal. Chem. 88 (2016) 974–980. https://doi.org/10.1021/acs.analchem.5b03732.

[14] T. Okuchi, H. Ohfuji, S. Odake, H. Kagi, S. Nagatomo, M. Sugata, H. Sumiya, Micromachining and surface processing of the super-hard nano-polycrystalline diamond by three types of pulsed lasers, Appl. Phys. a-Materials Sci. Process. 96 (2009) 833–842. https://doi.org/10.1007/s00339-009-5326-8.

[15] H. Ohfuji, T. Okuchi, S. Odake, H. Kagi, H. Sumiya, T. Irifune, Micro-/nanostructural investigation of laser-cut surfaces of single- and polycrystalline diamonds, Diam. Relat. Mater. 19 (2010) 1040–1051. https://doi.org/10.1016/j.diamond.2010.02.015.

[16] S.K. Sudheer, B. Kakadia, V.P.M. Pillai, G.A. Shafeev, A. V Simakin, Processing of natural diamond using nanosecond and picosecond lasers-relative merits and demerits - art. no. 68811G, Conf. Commer. Biomed. Appl. Ultrafast Lasers VIII. 6881 (2008) G8811–G8811. https://doi.org/10.1117/12.786994.

[17] T. V Kononenko, V.G. Ralchenko, I.I. Vlasov, S. V Garnov, V.I. Konov, Vlasov II, S. V Garnov, V.I. Konov, Ablation of CVD diamond with nanosecond laser pulses of UV-IR range, Diam. Relat. Mater. 7 (1998) 1623–1627. https://doi.org/10.1016/s0925-9635(98)00198-8.

[18] S. Gloor, W. Luthy, H.P. Weber, S.M. Pimenov, V.G. Ralchenko, V.I. Konov, A. V Khomich, UV laser polishing of thick diamond films for IR windows, Appl. Surf. Sci. 138 (1999) 135–139. https://doi.org/10.1016/s0169-4332(98)00493-0.

[19] E. Cappelli, G. Mattei, S. Orlando, F. Pinzari, P. Ascarelli, Pulsed laser surface modifications of diamond thin films, Diam. Relat. Mater. 8 (1999) 257–261. https://doi.org/10.1016/s0925-9635(98)00401-4.

[20] J. Li, C.L. Bentley, S. Tan, V. Mosali, R. Anisur, S.J. Cobb, S.-X. Guo, J. V. Macpherson, P.R. Unwin, A.M. Bond, J. Zhang, Sp2 Carbon Edge Effects on the Electrode Kinetics of the Ferrocene/Ferricenium Process in an Ionic Liquid at a Boron Doped Diamond Electrode, J. Phys. Chem. C. 123 (2019) 17397–17406. https://doi.org/10.1021/acs.jpcc.9b04519.

[21] Z.J. Ayres, S.J. Cobb, M.E. Newton, J. V. Macpherson, Quinone electrochemistry for the comparative assessment of sp2 surface content of boron doped diamond electrodes, Electrochem. Commun. 72 (2016) 59–63.

https://doi.org/10.1016/j.elecom.2016.08.024.

[22] M.L. Hicks, A.C. Pakpour-Tabrizi, R.B. Jackman, Diamond Etching Beyond 10 μm with Near-Zero Micromasking, Sci. Rep. 9 (2019) 17–19. https://doi.org/10.1038/s41598-019-51970-8.

[23] D.R. Lide, CRC handbook of chemistry and physics, CRC press, 2004.

[24] R. Windholz, P.A. Molian, Nanosecond pulsed excimer laser machining of chemically vapour-deposited diamond and graphite: Part II. Analysis and modelling, J. Mater. Sci. 33 (1998) 523–528.

[25] S. Preuss, M. Stuke, Subpicosecond Ultraviolet-Laser Ablation of Diamond - Nonlinear Properties at 248 Nm and Time-Resolved Characterization of Ablation Dynamics, Appl. Phys. Lett. 67 (1995) 338–340. https://doi.org/Doi 10.1063/1.115437.

[26] D. Ramanathan, P. a. Molian, Micro- and sub-micromachining of type IIa single crystal diamond using a Ti : Sapphire femtosecond laser, J. Manuf. Sci. Eng. Asme. 124 (2002) 389–396. https://doi.org/10.1115/1.1459083.

[27] M. Shinoda, R.R. Gattass, E. Mazur, Femtosecond laser-induced formation of nanometer-width grooves on synthetic single-crystal diamond surfaces, J. Appl. Phys. 105 (2009) 053102. https://doi.org/10.1063/1.3079512.

[28] S. Su, J. Li, G.C.B. Lee, K. Sugden, D. Webb, H. Ye, Femtosecond laser-induced microstructures on diamond for microfluidic sensing device applications, Appl. Phys. Lett. 102 (2013) 231913. https://doi.org/10.1063/1.4811170.

[29] V. V Kononenko, T. V Kononenko, S.M. Pimenov, M.N. Sinyavskii, V.I. Konov, F. Dausinger, Effect of the pulse duration on graphitisation of diamond during laser ablation, Quantum Electron. 35 (2005) 252–256. https://doi.org/10.1070/QE2005v035n03ABEH002900.

[30] M. Wu, B. Guo, Q. Zhao, P. He, Z. Zeng, J. Zang, The influence of the ionization regime on femtosecond laser beam machining mono-crystalline diamond, Opt. Laser Technol. 106 (2018) 34–39. https://doi.org/10.1016/j.optlastec.2018.03.031.

[31] S. Osswald, G. Yushin, V. Mochalin, S.O. Kucheyev, Y. Gogotsi, Control of sp(2)/sp(3) carbon ratio and surface chemistry of nanodiamond powders by selective oxidation in air, J. Am. Chem. Soc. 128 (2006) 11635–11642. https://doi.org/10.1021/ja063303n.

[32] A. Krueger, D. Lang, Functionality is key: Recent progress in the surface modification of nanodiamond, Adv. Funct. Mater. 22 (2012) 890–906. https://doi.org/10.1002/adfm.201102670.

[33] T.L. Read, S.J. Cobb, J. V. Macpherson, An sp 2 Patterned Boron Doped Diamond Electrode for the Simultaneous Detection of Dissolved Oxygen and pH, ACS Sensors. 4 (2019) 756–763. https://doi.org/10.1021/acssensors.9b00137.

[34] S. Garcia-Segura, E. Vieira dos Santos, C.A. Martínez-Huitle, Role of sp3/sp2 ratio on the electrocatalytic properties of boron-doped diamond electrodes: A mini review, Electrochem. Commun. 59 (2015) 52–55. https://doi.org/10.1016/j.elecom.2015.07.002.

[35] S.J. Cobb, Z.J. Ayres, M.E. Newton, J. V. Macpherson, Deconvoluting surface-bound quinone proton coupled electron transfer in unbuffered solutions: towards a universal voltammetric pH electrode, J. Am. Chem. Soc. 141 (2019) 1035–1044. https://doi.org/10.1021/jacs.8b11518.

[36] F. Cleri, P. Keblinski, L. Colombo, D. Wolf, S.R. Phillpot, On the electrical activity of sp^2 -bonded grain boundaries in nanocrystalline diamond, Europhys. Lett. 46 (1999) 671–677. https://doi.org/10.1209/epl/i1999-00318-5.

[37] X.Z. Liao, R.J. Zhang, C.S. Lee, S.T. Lee, Y.W. Lam, The influence of boron doping on the structure and characteristics of diamond thin films, Diam. Relat. Mater. 6 (1997) 521–525. https://doi.org/10.1016/S0925-9635(96)00640-1.

[38] A.J. Lucio, R. Meyler, M.A. Edwards, J. V Macpherson, Investigation of sp2-carbon pattern geometry in boron doped diamond electrodes for the electrochemical quantification of hypochlorite at high concentrations, (2020). https://doi.org/10.1021/acssensors.9b02444.

[39] F. Picollo, A. Battiato, E. Bernardi, A. Marcantoni, A. Pasquarelli, E. Carbone, P. Olivero, V. Carabelli, Microelectrode Arrays of Diamond-Insulated Graphitic Channels for Real-Time Detection of Exocytotic Events from Cultured Chromaffin Cells and Slices of Adrenal Glands, Anal. Chem. 88 (2016) 7493–7499. https://doi.org/10.1021/acs.analchem.5b04449.

[40] F. Picollo, A. Battiato, E. Carbone, L. Croin, E. Enrico, J. Forneris, S. Gosso, P. Olivero, A. Pasquarelli, V. Carabelli, Development and Characterization of a Diamond-Insulated

Graphitic Multi Electrode Array Realized with Ion Beam Lithography, Sensors . 15 (2015). https://doi.org/10.3390/s150100515.

[41] H. Kozak, A. Kromka, E. Ukraintsev, J. Houdkova, M. Ledinsky, M. Vaněček, B. Rezek, Detecting sp2 phase on diamond surfaces by atomic force microscopy phase imaging and its effects on surface conductivity, Diam. Relat. Mater. 18 (2009) 722–725. https://doi.org/10.1016/j.diamond.2009.02.010.

[42] J.Y. Shim, H.K. Baik, Effect of non-diamond carbon etching on the field emission property of highly sp2 nanocrystalline diamond films, Diam. Relat. Mater. 10 (2001) 847–851. https://doi.org/10.1016/S0925-9635(01)00378-8.

[43] A. Stacey, N. Dontschuk, J.P. Chou, D.A. Broadway, A.K. Schenk, M.J. Sear, J.P. Tetienne, A. Hoffman, S. Prawer, C.I. Pakes, A. Tadich, N.P. de Leon, A. Gali, L.C.L. Hollenberg, Evidence for Primal sp 2 Defects at the Diamond Surface: Candidates for Electron Trapping and Noise Sources, Adv. Mater. Interfaces. 6 (2019) 1–8. https://doi.org/10.1002/admi.201801449.

[44] N.G. Ferreira, E. Abramof, E.J. Corat, V.J. Trava-Airoldi, Residual stresses and crystalline quality of heavily boron doped diamond films analysed by micro-Raman spectroscopy and X-ray diffraction, Carbon N. Y. 41 (2003) 1301–1308. https://doi.org/doi:10.1016/S0008-6223(03)00071-X.

[45] L.A. Hutton, J.G. Iacobini, E. Bitziou, R.B. Channon, M.E. Newton, J. V Macpherson, Examination of the Factors Affecting the Electrochemical Performance of Oxygen-Terminated Polycrystalline Boron-Doped Diamond Electrodes, Anal. Chem. 85 (2013) 7230–7240. https://doi.org/10.1021/ac4010421.

[46] W.R. Carmody, Easily prepared wide range buffer series, J. Chem. Educ. 38 (1961) 559. https://doi.org/10.1021/ed038p559.

[47] K. Das, V. Venkatesan, K. Miyata, D.L. Dreifus, J.T. Glass, A review of the electrical characteristics of metal contacts on diamond, Thin Solid Films. 212 (1992) 19–24. https://doi.org/10.1016/0040-6090(92)90494-V.

[48] D. Nečas, P. Klapetek, Gwyddion: An open-source software for SPM data analysis, Cent. Eur. J. Phys. 10 (2012) 181–188. https://doi.org/10.2478/s11534-011-0096-2.

[49] R.M. Langford, T.X. Wang, D. Ozkaya, Reducing the resistivity of electron and ion beam assisted deposited Pt, Microelectron. Eng. 84 (2007) 784–788.

https://doi.org/10.1016/j.mee.2007.01.055.

[50] J.A. Hunt, D.B. Williams, Electron energy-loss spectrum-imaging, Ultramicroscopy. 38 (1991) 47–73. https://doi.org/10.1016/0304-3991(91)90108-I.

[51] Y. Sato, M. Bugnet, M. Terauchi, G.A. Botton, A. Yoshiasa, Diamond & Related Materials Heterogeneous diamond phases in compressed graphite studied by electron energy-loss spectroscopy, Diam. Relat. Mater. 64 (2016) 190–196. https://doi.org/10.1016/j.diamond.2016.02.010.

[52] A.L. Hamon, J. Verbeeck, D. Schryvers, J. Benedikt, R.M.C.M.V.D. Sanden, ELNES study of carbon K-edge spectra of plasma deposited carbon films, J. Mater. Chem. 14 (2004) 2030–2035. https://doi.org/10.1039/b406468m.

[53] A.J. Papworth, C.J. Kiely, A.P. Burden, S.R.P. Silva, G.A.J. Amaratunga, Electron-energy-loss spectroscopy characterization of the sp2 bonding fraction within carbon thin films, Phys. Rev. B - Condens. Matter Mater. Phys. 62 (2000) 12628–12631. https://doi.org/10.1103/PhysRevB.62.12628.

[54] R.F. Edgerton, Electron Energy-Loss Spectroscopy in the Electron Microscope, 2nd editio, Plenum Press, 1996.

[55] J. Bruley, D.B. Williams, J.J. Cuomo, D.P. Pappas, Quantitative near-edge structure analysis of diamond-like carbon in the electron microscope using a two-window method, J. Microsc. 180 (1995) 22–32. https://doi.org/10.1111/j.1365-2818.1995.tb03653.x.

[56] R. Brydson, Z. Zhili, A. Brown, Revisiting the determination of carbon sp2/sp3 ratios via analysis of the EELS carbon K-edge, Yaoxue Xuebao. 36 (2001) 92–95. https://doi.org/10.1007/978-3-540-85156-1.

[57] W. Zhu, X.H. Wang, D.J. Pickrell, A.R. Badzian, R. Messier, The Oxidation of CVD Diamond Films, Carbon N. Y. 28 (1990) 796. https://doi.org/10.1016/0008-6223(90)90302-F.

[58] A. Kriele, O.A. Williams, M. Wolfer, J.J. Hees, W. Smirnov, C.E. Nebel, Formation of nano-pores in nano-crystalline diamond films, Chem. Phys. Lett. 507 (2011) 253–259. https://doi.org/10.1016/j.cplett.2011.03.089.

[59] A.A. Zavitsas, The relation between bond lengths and dissociation energies of carbon-carbon bonds, J. Phys. Chem. A. 107 (2003) 897–898. https://doi.org/10.1021/jp0269367.

[60] S. Michaelson, R. Akhvlediani, A. Hoffman, Hydrogen bonding configuration and thermal stability of ambient exposed and in situ hydrogenated polycrystalline diamond surfaces studied by high resolution electron energy loss spectroscopy, Phys. Chem. Chem. Phys. 13 (2011) 11471–11480. https://doi.org/10.1039/c1cp00019e.

[61] S. Michaelson, R. Akhvlediani, A. Hoffman, Hydrogenation and thermal stability of nano- and microcrystalline diamond films studied by vibrational electron spectroscopy, J. Appl. Phys. 104 (2008). https://doi.org/10.1063/1.3000662.

[62] D.F. Talbot-Ponsonby, M.E. Newton, J.M. Baker, G.A. Scarsbrook, R.S. Sussmann, A.J. Whitehead, S. Pfenninger, Multifrequency EPR, H-1 ENDOR, and saturation recovery of paramagnetic defects in diamond films grown by chemical vapor deposition, Phys. Rev. B. 57 (1998) 2264–2270. https://doi.org/10.1103/PhysRevB.57.2264.

[63] D.F. Talbot-Ponsonby, M.E. Newton, J.M. Baker, G.A. Scarsbrook, R.S. Sussmann, A.J. Whitehead, EPR and optical studies on polycrystalline diamond films grown by chemical vapor deposition and annealed between 1100 and 1900 K, Phys. Rev. B. 57 (1998) 2302–2309. https://doi.org/10.1103/PhysRevB.57.2302.

[64] P.W. May, Diamond Thin Films : A 21st-Century Material Author (s): Paul W . May Source : Philosophical Transactions : Mathematical , Physical and Engineering Sciences, Vol . 358 , No . 1766 , Science into the Next Millennium : Young Scientists Give Their Visions, 358 (2000) 473–495.

[65] Z.J. Ayres, J.C. Newland, M.E. Newton, S. Mandal, O.A. Williams, J. V. Macpherson, Impact of chemical vapour deposition plasma inhomogeneity on the spatial variation of sp 2 carbon in boron doped diamond electrodes, Carbon N. Y. 121 (2017) 434–442. https://doi.org/10.1016/j.carbon.2017.06.008.

Graphical Abstract: